Nearest-neighbor Gaussian Process Emulation for Tensor Responses in Freeze Nano 3D Printing of Energy Products

Luis Javier Segura

Department of Industrial and Systems Engineering University at Buffalo, the State University of New York Buffalo, NY 14260, U.S.A. lseguras@buffalo.edu

Guanglei Zhao

Department of Industrial and Systems Engineering University at Buffalo, the State University of New York Buffalo, NY 14260, U.S.A. guanglei@buffalo.edu ASME Membership

Chi Zhou

Department of Industrial and Systems Engineering University at Buffalo, the State University of New York Buffalo, NY 14260, U.S.A. chizhou@buffalo.edu ASME Membership

Hongyue Sun¹

Department of Industrial and Systems Engineering University at Buffalo, the State University of New York Buffalo, NY 14260, U.S.A. hongyues@buffalo.edu ASME Membership

1

¹ Contact author: hongyues@buffalo.edu

ABSTRACT

Energy 3D printing processes have enabled the manufacturing of energy storage devices with complex structures, high energy density, and high power density. Among these processes, Freeze Nano Printing (FNP) has risen as a promising process that seamlessly integrates freeze casting and inkjet printing processes. FNP can fabricate flexible energy products with both macroscale and microscale features, resulting in good mechanical and electrical properties with a lightweight structure of the final product. However, quality problems are among the biggest barriers that FNP, and other 3D printing processes, need to overcome. In particular, the droplet solidification time in FNP governs the thermal distribution, and subsequently determines the product solidification, formation and quality. To describe the solidification time, physical-based heat transfer model is built. But it is computationally inefficient for real-time solidification time prediction during the printing process. Therefore, the objective of this work is to build an efficient emulator for the physical model. We need to face several challenges unaddressed before: 1) the solidification time at various locations, which is a tensor response, needs to be modeled and predicted; 2) the construction and evaluation of the emulator at new process settings need to be quick and accurate, to quide potential process adjustments. Here, we integrate joint tensor decomposition and Nearest Neighbor Gaussian Process (NNGP) to construct an efficient tensor response emulator with process settings as inputs. Specifically, structured joint tensor decomposition decomposes the tensor responses at various process settings into the setting-specific core tensors and shared low dimensional factorization matrices. Then, each independent entry of the core tensor is modeled with a NNGP, which addresses the computationally intensive model estimation problem by sampling the nearest neighborhood samples. Finally, tensor reconstruction is performed to make predictions of solidification time for new process settings. The proposed framework is demonstrated by emulating the physical model of FNP, and compared with alternative tensor regression models.

Keywords: Energy 3D Printing, Freeze Nano Printing, Gaussian Process, Nearest Neighbor Gaussian Process,
Tensor Response Emulation.

INTRODUCTION

Micro-energy storage devices such as batteries and supercapacitors that possess high energy density and high power density properties are fundamental for smart and wearable micro-devices in domains such as the Internet of Things (IoT) and medicine [1, 2]. However, as reported by the U.S. defense logistics agency, the current energy storage materials and devices can have either high energy density or high-power density, but they do not have both properties [3]. In order to solve this issue, several approaches such as energy harvesting, element doping, and surface functionalization have been tested [4, 5]. For instance, piezoelectric and triboelectric nanogenerators are used for energy harvesting. These devices convert mechanical motion into electricity to replenish the energy of conventional batteries and supercapacitors, thus compensating their limited energy storage capacity [4]. Additionally, element doping and surface functionalization are effective strategies to increase the capacitance of electrode materials for asymmetric capacitors. However, these strategies require external agents (e.g., hematite and polyurethane) for modifying the electrical properties and surface properties of the electrode materials [5]. Nevertheless, these methods do not fully acquire the desired high energy density and high power density; there is always a tradeoff between them.

The advent of 3D printing has generated important progress towards the manufacturing of complex structures to improve the energy storage devices. It has risen as a promising technique to build architectures that can efficiently achieve the high energy density and high power density of batteries and supercapacitors [6]. 3D printing techniques, varying from material extrusion (e.g., Fused Deposition Modeling, FDM),

material jetting (e.g., inkjet printing), and powder bed fusion (e.g., Selective Laser Melting, SLM), are capable of fabricating functional parts layer by layer and have been widely used to produce customized products [7]. Among them, material extrusion and material jetting have been successfully demonstrated to produce energy products, such as fuel cells, supercapacitors and batteries, with outstanding electrical properties [8, 9].

Lately, a novel 3D printing technique, Freeze Nano Printing (FNP), has been developed to produce energy storage devices [10]. FNP integrates inkjet printing with freeze casting to produce complex shaped Graphene Aerogels (GAs) with both macroscale and microscale feature printing capabilities. Fig. 1 shows an illustration of the FNP process. Firstly, Graphene Oxide (GO) ink with the concentration of around 0.5 mg/ml is prepared to guarantee the GO ice structure (Step 1). The GO ink droplets are controllably ejected to a cold substrate through a nozzle, following a designed path to form the printed layers (Steps 2-3). Particularly, the droplets are supplied by a piezoelectric nozzle that controls the demand of the aqueous solution. The GO droplets are instantly frozen and the ice crystals are formed once the droplets are deposited onto the cold substrate at an ambient temperature of around -20 °C. The 3D printed part is then submerged in liquid nitrogen to be firstly frozen in critical cooling condition at around -190 $^{\circ}C$ and subsequently placed in an ultralow temperature chamber at -80 $^{\circ}C$ for 24 hours to enable further ice crystallization (Step 4). To remove water, the three-dimensional graphene structure is freeze dried for 48 hours (Step 5). Finally, the printed part undergoes thermal reduction at 1000 $^{\circ}C$ for 1 hour in a tube furnace with hydrogen atmosphere to obtain the ultralight 3D printed structure (Step 6) [11].

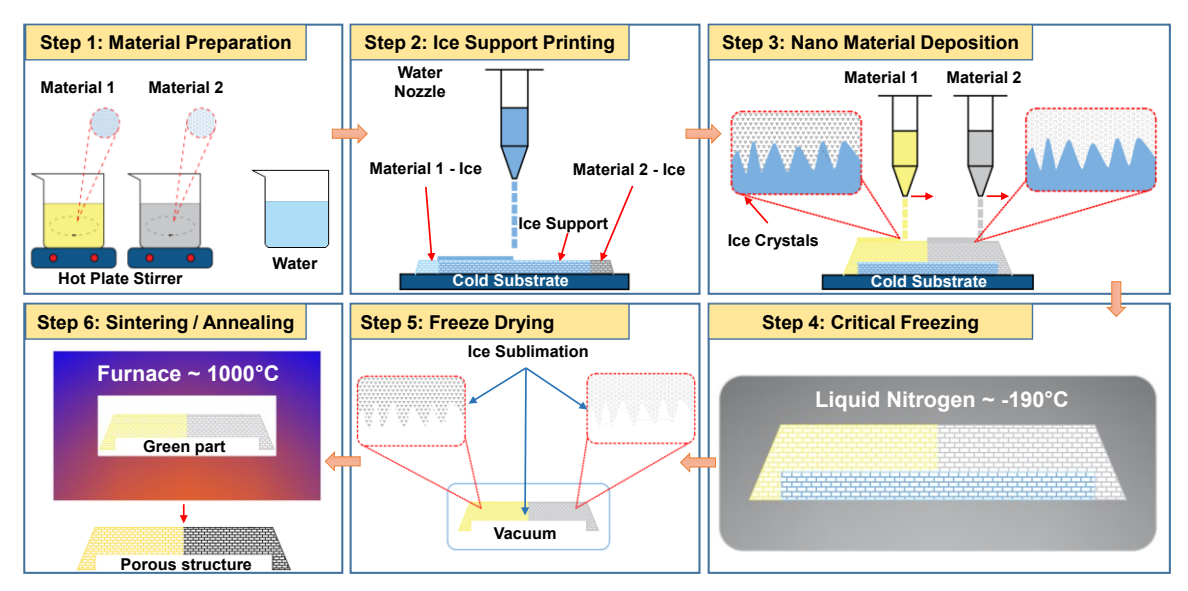


Fig. 1 An Illustration of the Freeze Nano Printing Process [10]

The FNP has been proved to possess a great potential to achieve structures that can improve both energy density and power density for energy products due to hierarchical porous structures balancing mass transport, ion diffusion, and diffusion length [10]. Different from continuous inkjet technique to print graphene structures by adjusting the rheological properties, namely shear-thinning behavior of non-Newtonian GA inks, FNP uses a low viscous Newtonian GO suspension that performs the printing droplet by droplet until the layers are formed. This is beneficial to improving the bonding strength among layers since newly deposited not-yet-frozen droplets melt the already frozen surface. Then, the two layers are refrozen due to ambient temperature (-20 °C) [12].

Current studies on 3D printing of energy products have focused on proof-ofconcept demonstration, yet do not pay attention to the quality and repeatability of the printed products. In fact, limited quality and high uncertainty remain big challenges for 3D printing processes [13]. In FNP, thermal management of droplet solidification time is a critical quality-determining factor. It will govern the waiting time between layers and consequently affect the part bonding strength and dimensional accuracy. The waiting time will also affect the productivity of the printing process. It is therefore crucial to study the solidification time to determine the optimal waiting time. However, studying the droplet solidification time is an intricate problem due to the complex thermal interactions among the droplets, substrate, and ambient. In addition, newly deposited GO suspension droplets undergo phase changes during solidification due to the release of latent heat of previously deposited layers. This will prevent the newly deposited droplets from freezing, thus affecting the macro- and micro-structures. Moreover, the droplets solidification is dependent on the process parameters (e.g., layer thickness) and material properties (e.g., heat transfer coefficient).

Since graphene is a very expensive material (\$250/g), it is impractical to study the droplet solidification time and optimize the waiting time in a trial-and-error approach. Therefore, a physical-based thermal model is proposed to describe the droplet thermal interactions and solidifications as well as to determine the waiting time [14]. Nonetheless, the physical-based model can be computationally inefficient for moderate to large parts, and they can hardly be used for real-time droplet solidification study and waiting time determination. Therefore, the objective of this work is to propose an efficient and accurate emulator for the physical-based modeling results of high dimensional droplet solidification time. The droplet solidification time at various locations form a tensor

response for the emulator, with the process settings as predictors. The Gaussian Process (GP) is widely used for physical model emulation and calibration [15, 16, 17], due to its flexibility to capture the nonlinear relationships usually represented by the physical-based differential equations. However, most existing GP emulators are designed for scalar responses and are computationally expensive during model training and evaluation. Recently, some endeavors are spent for multivariate and high-dimensional responses in GP emulation [16, 17], but they are either not applicable to general tensor responses or not efficient for real-time solidification prediction. Therefore, two challenges need to be addressed in the proposed emulator: 1) the modeling of the tensor responses (i.e., solidification time); 2) the efficient construction and evaluation of the emulator at new process settings.

In this paper, we integrate joint tensor decomposition and Nearest Neighbor Gaussian Process (NNGP) for the physical model emulation. Tensor decomposition is widely used for sparse representation of tensors [18]. While most tensor decomposition methods are for a single tensor, here, we jointly decompose multiple tensor responses at various process settings with joint tensor decomposition [19, 20]. As a result, the tensor responses are represented with the outer product of corresponding vectors in the shared low dimensional factorization matrices and entries in the setting-specific core tensor [19, 20]. In particular, we design a structured joint tensor decomposition for the solidification time in FNP so that the core tensor is superdiagonal (see details in the Proposed Method and Case Study sections). Other structures of the joint tensor decomposition can be deployed for other applications. After the joint tensor decomposition, we then model the

independent entries in the core tensors with NNGP. NNGP performs the model estimation based on local nearest neighbors for each sample, and enjoys significant computational savings compared with the conventional GP model [21].

As will be demonstrated in the Case Study section, the proposed emulator is able to yield good prediction results and can have very fast solidification time predictions. Such a model is applicable to the tensor responses emulation from the physical model and can be widely used for other 3D printing processes, such as the thermal simulation in SLM and droplet simulation in inkjet printing [22, 23]. Although there are several methods to model tensor responses [24], to the extent of our knowledge, this is the first study dedicated to emulating the physical model with tensor responses for 3D printing processes. The proposed model is extensively compared to alternative models shown in [24, 25, 26], in which regression models are used for tensor responses modeling. The results showed that our proposed model outperformed the accuracy of the other alternatives.

The organization of this paper is as follows. In the next section, we present the relevant literature on 3D printing of energy products, quality modeling, and control of 3D printed parts, and tensor decomposition and tensor response modeling for manufacturing. We then illustrate the proposed method for the tensor response emulation. After that, the proposed method is demonstrated in an FNP process for the solidification time prediction. Finally, we conclude the paper and discuss the future work.

STATE-OF-THE-ART

3D printing of anode, cathode, and electrolyte, which are the main components of energy storage devices, has shown promising results to improve the performance of batteries and supercapacitors. However, 3D printing of these devices is a non-trivial task, and researchers have devoted lots of efforts on this topic [12]. For instance, a Li-Ion microbattery was developed in [27]. Interdigitated electrodes were integrated on a submillimeter scale, where Li₄Ti₅O₁₂ (LTO) and LiFePO₄ (LFP) were used as anode and cathode electrodes, respectively. The authors claimed their device yielded the highest areal energy and power densities reported to date. Additionally, GO-based electrode inks for Li-Ion batteries were 3D printed in [28]. The printed GO porous structure benefits the high areal surface, consequently more LTO and LFP nanoparticles can be allocated to increase the energy storage capacity. Other attempts to improve the performance of energy storage devices through the addition of graphene nanoplates and extrusion of silicon, activated carbon, and gel electrolyte, are shown in [29, 30]. Although there is a lot of work related to 3D printing for energy storage devices, these efforts are at the proofof-concept fabrication and the product integrity, quality, and productivity have not been fully considered.

Several 3D printed products' defects are investigated by using data-driven, physical models, or hybrid approaches. To model and quantify the layer-wise spatial evolution of porosity in 3D printed parts, an augmented layer-wise spatial log Gaussian cox process was proposed in [31]. A systematic model to predict part shrinkage and an optimal shrinkage compensation plan to achieve dimensional accuracy were presented in [32]. The dimensional variation was also studied by extracting 3D point cloud data from

3D printed parts in [33]. Moreover, approaches based on physical models are utilized to improve quality in 3D printing parts. For instance, to improve mechanical properties, surface finish, and dimensional accuracy in 3D printed parts, physical models based on heat transfer and fluid dynamics were presented in [14, 34]. These models can be timeconsuming to be evaluated and may suffer from model uncertainty. Hybrid approaches allow the development of emulation/calibration models by integrating data-driven and physical-based models. For instance, to predict the parts' porosity at any given process settings in SLM of metallic parts, a GP model was used to characterize process porosity [35]. Li et al. used a multivariate GP model for the physical model calibration [36]. See also [37] for an FNP application in distributed printers. Nevertheless, the high dimensional matrix/tensor responses are rarely studied in the existing emulation/calibration models. Moreover, the computational requirements for GP model can be high, especially for large datasets. To accelerate the GP model learning process, NNGP provides a scalable alternative by using local information from few nearest neighbors [38], and will be explored in this paper.

Recently, much attention was drawn to the tensor decomposition and tensor responses modeling. Tensor decomposition is widely used for dimensionality reduction of tensor objects in denoising, completion, etc., and is also crucial for later analysis with methods such as regression, GP, and NNGP [18]. The tensor decomposition techniques, such as Candecomp/Parafac (CP) and Tucker decomposition, have a sparse representation of the tensor data [39]. While the majority of tensor decompositions are for a single tensor [18], the joint tensor decompositions are recently investigated [19, 20],

and used for manufacturing applications. For instance, a regularized tensor regression was proposed for the turning process optimization based on the point cloud measurement of cylinder parts as predictors and dimensional accuracy as the response [40]. Additionally, a method to quickly classify part geometrical integrity with minimal point cloud data in FDM was proposed in [41]. See also [42] for an application in process monitoring. The above methods use tensor as predictors, rather than responses, and cannot be used in the FNP emulation. Currently, the tensor responses were modeled in some medical applications. For instance, Sparse TensOr REsponse regression (STORE), with a tensor response and vector predictor, was proposed in [24]. Sparse Ordinary Least Squares (Sparse OLS) was presented in [25]. This method first vectorizes the tensor response, and then fits a regularized multivariate regression with the Lasso penalty. Additionally, Higher-Order Low-Rank Regression (HOLRR) method, which enforces a lowrank tensor structure, was demonstrated in [26]. In this work, we integrate the joint tensor decomposition and NNGP model to handle the matrix/tensor responses from the physical model of FNP and then compare our proposed framework to alternative models in [24, 25, 26].

PROPOSED METHOD

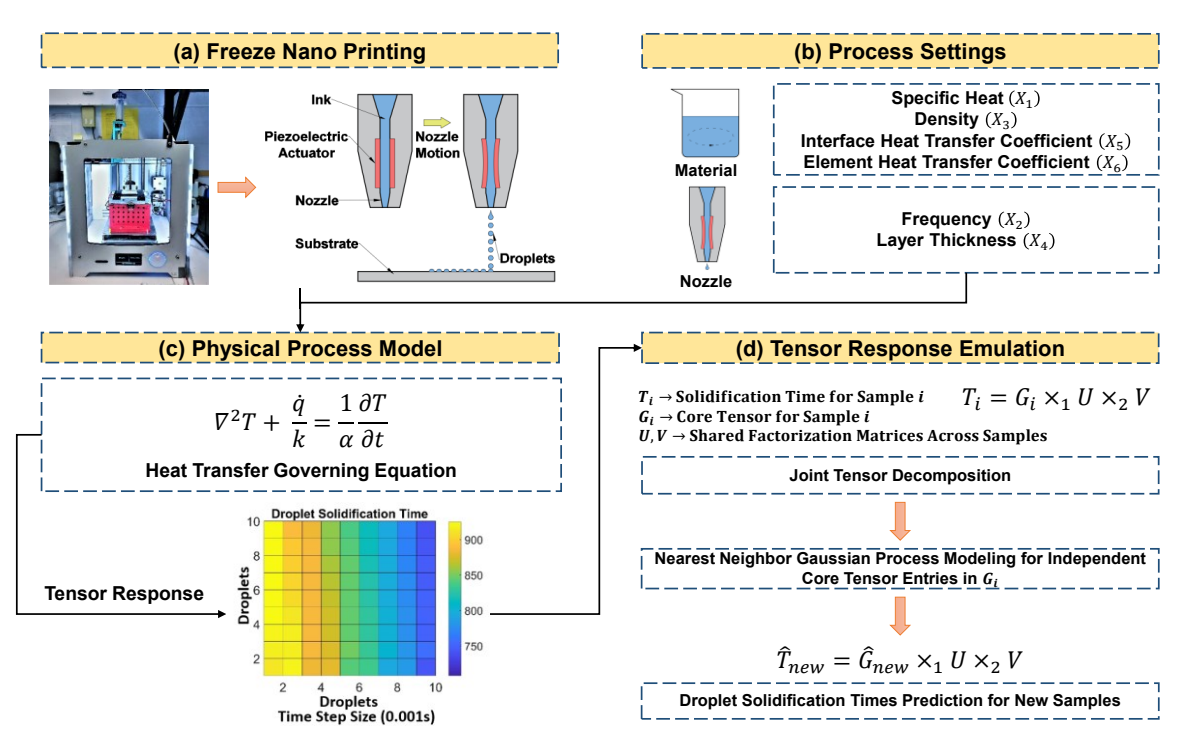


Fig. 2 An Illustration of the Proposed Framework: (a) Scheme of the FNP setup, (b) Process settings for the physical model input simulation, (c) Physical heat transfer process model, and (d) Tensor response modeling via joint tensor decomposition and NNGP

and X_6 in Fig. 2 (b)) and process parameters (X_2 and X_4 in Fig. 2 (b)). The solidification times at multiple process settings are factorized by structured joint tensor decomposition, as illustrated in Fig. 2 (d), where the core tensor is superdiagonal. After the tensor decomposition, we model each independent entry at a fixed coordinate of the core tensors from different process settings with a NNGP model. Finally, after separately training the NNGP models, the droplet solidification time can be predicted by the reconstruction from the predicted core tensor entries and the factorization matrices. The reconstructed tensor will be compared with the droplet solidification time simulated from the physical model.

In the proposed method, the simulation data generation from the physical model, the joint tensor decomposition, and the training of NNGP models are performed offline.

Once the models are trained, the predictions of the solidification time at new process settings from NNGP can be performed much faster than executing the physical model. Thus, the real-time process optimization and control could be feasible, which are out of the scope in this paper and will be investigated in the future. The following section is dedicated to explaining the details of the proposed method.

Joint Tensor Decomposition

Tensor decomposition is a powerful dimensional reduction technique. The basic idea of tensor decomposition is to approximate the high dimensional tensor with the tensor product of low dimensional factorization matrices (e.g., U and V in Fig. 2 (d)) and core tensor (e.g., G in Fig. 2 (d)). Without loss of generality, we illustrate the method with a third order tensor $T \in \mathbb{R}^{I \times J \times K}$. In general, T can be decomposed by CP decomposition $T \approx \tilde{T}^{CP} = \sum_r g_r^{CP} u_r^{CP} \circ v_r^{CP} \circ w_r^{CP} = \llbracket G^{CP}; U^{CP}, V^{CP}, W^{CP} \rrbracket$ or Tucker decomposition $T \approx \tilde{T}^{Tucker} = \sum_{l} \sum_{m} \sum_{n} G^{Tucker}(l, m, n) U^{Tucker}(i, l) V^{Tucker}(j, m) W^{Tucker}(k, n) =$ $\llbracket G^{Tucker}, U^{Tucker}, V^{Tucker}, W^{Tucker} \rrbracket$ [18]. For CP decomposition, $U^{CP} = \{u_r^{CP}, \forall r\} \in$ $R^{I \times R}$, $V^{CP} = \{v_r^{CP}, \forall r\} \in R^{J \times R}$, and $W^{CP} = \{w_r^{CP}, \forall r\} \in R^{K \times R}$ are factorization matrices, $G^{CP} = \{g_r^{CP}, \forall r\} \in R^{R \times R \times R}$ is a superdiagonal core tensor that specifies the weight for each rank-one tensor $u_r^{CP} \circ v_r^{CP} \circ w_r^{CP}$ to reconstruct T, and the rank R is the minimum number of rank-one tensors to represent T (i.e., $r=1,\cdots,R$) (See Fig. 3 for an illustration). \circ is the outer product. For Tucker decomposition, $U^{Tucker} \in R^{I \times L}$, $V^{Tucker} \in$ $R^{J\times M}$, and $W^{Tucker} \in R^{K\times N}$ are factorization matrices, $G^{Tucker} \in R^{L\times M\times N}$ is the core tensor. These two approaches are the generalized form of each other [18]. In this work, we use the CP decomposition to represent the high dimensional tensor responses. Throughout the paper, we drop *CP* in the above notation, and have the decomposition $T\approx \tilde{T}=\sum_r g_r u_r\circ v_r\circ w_r=\llbracket G;U,V,W\rrbracket.$

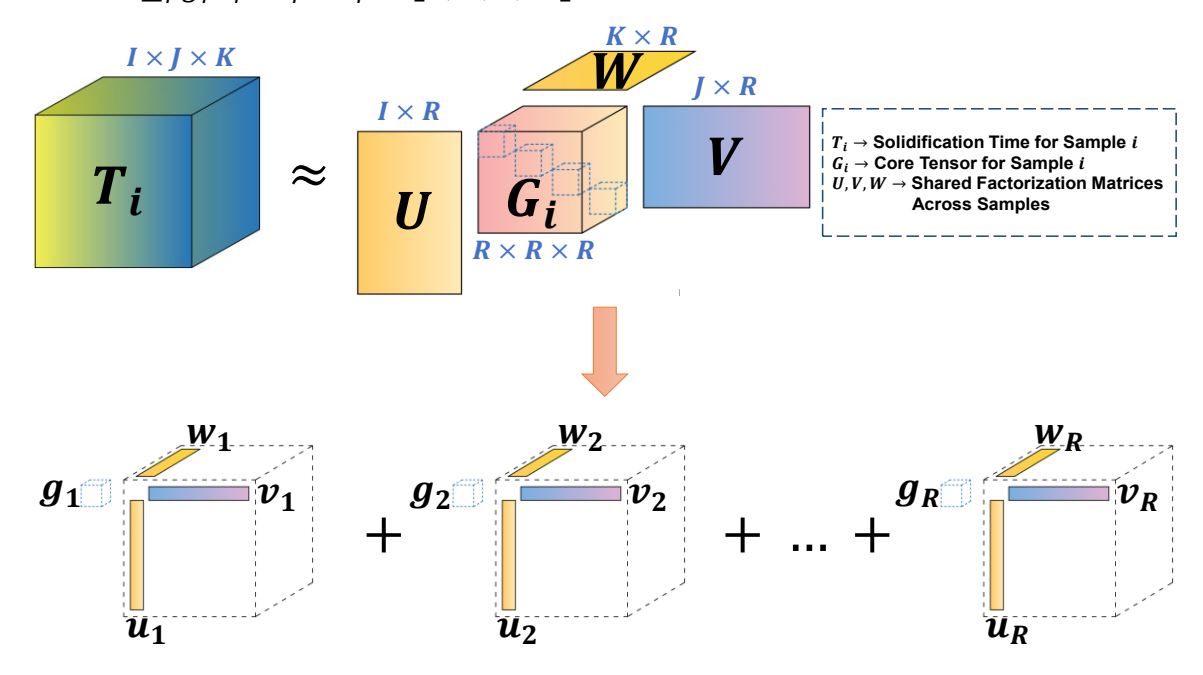


Fig. 3 A Schematic Illustration of the Joint Tensor Decomposition

To represent the droplet solidification time at various process settings, we use the joint tensor decomposition, where the factorization matrices U, V and W for T_i 's at various process settings are shared, as illustrated on the top of Fig. 3. We can therefore characterize the tensors with G_i given the shared decomposition matrices U, V and W [20]. In particular, the joint tensor decomposition can be solved via,

$$\min \frac{1}{n} \sum_{i=1}^{n} ||T_i - [G_i; U, V, W]||_F$$
 (1)

where $\|\cdot\|_F$ is the Frobenius norm, n is the number of samples, and $[\![\cdot]\!]$ is the tensor product. The problem is solved with nonlinear least square (i.e., trust-region Quasi-Newton methods), where U,V and W are initialized with random matrices [43]. The rank R can be determined so that the variation explained in the approximation tensor $\tilde{T}_i, \forall i$ is larger than a threshold percentage of the variation in the raw tensor T_i . The rank R

needed is usually a small number compared with the original dimensionality of the tensor. Such a selection approach is also widely used in determining the number of principal components in principal component analysis [44]. After the joint tensor decomposition, other than modeling the raw tensor responses directly, the emulation problem can be simplified to model each $g_{i,r}$'s in G_i with a NNGP model, $r=1,\cdots,R$, respectively. This is because the non-zero entries in the core tensor only appear in the superdiagonal and can be modeled independently. For other applications, one can use other tensor decomposition formulations, and separately model the orthogonal entries in the core tensor.

Nearest Neighbor Gaussian Process (NNGP) Emulation

GP models provide a very flexible non-parametric approach to capture the spatial patterns [38]. In our previous work [45], GP emulation was used for the tensor response modeling of the solidification time (after the joint tensor decomposition) in FNP with a relatively small sample size. The GP emulator can deal with the tensor response, but the prediction error is not small enough for the future process optimization. To improve the model performance, in this work, we increase the number of samples from the physical model simulation. This will make GP model not applicable, since GP model is computationally intensive for median and large sample sizes. To ameliorate this problem, a NNGP model using an extension of the Vecchia approximation [46] is used to build the emulator [38].

In general, for a certain rank r of the core tensors after the joint tensor decomposition, the GP model $g_{i,r}$ for G_i at the i-th sample is

$$g_{i,r}(\mathbf{x}_i) = m_{i,r}(\mathbf{x}_i) + \omega_{i,r}(\mathbf{x}_i) + \varepsilon_{i,r}(\mathbf{x}_i), \tag{2}$$

where x_i contains the physical model inputs, such as layer thickness, droplet frequency, and the detailed values of these inputs are provided in Table 1. $m_{i,r}(x_i) = x_i^T \boldsymbol{\beta}_r$ is the mean function capturing the mean effect of x_i on $g_{i,r}$, and $\boldsymbol{\beta}_r$ is the model parameters for the mean effect; $\omega_{i,r}(x_i)$ follows a GP $\omega_{i,r}(x_i) \sim GP\left(0, C_r(x_i, x_i')\right)$, where $C_r(x_i, x_i') = \sigma_r^2 exp\left(-\sum_j \phi_{r,j} \left\|x_{i,j} - x_{i,j}'\right\|\right)$ is the covariance function capturing the spatial relationship of samples. $\phi_{r,j}$ is used to adjust the weight of each direction j while calculating the distance, and σ_r^2 is a scaling parameter. For instance, based on the covariance function, the close-by samples in the process settings are highly correlated, whereas the far-away samples tend to have lower correlation. $\varepsilon_{i,r}(x_i) \sim N(0, \tau_r^2)$ is the error term. The unknown parameters in the model are $\boldsymbol{\theta}_r = \{\boldsymbol{\beta}_r, \sigma_r^2, \phi_{r,j}, \tau_r^2, \forall j\}$, and can be learned from the Markov Chain Monte Carlo (MCMC) sampling from the posterior distribution [47]

$$p\left(\boldsymbol{\Theta}_r|g_{i,r}(\boldsymbol{x}_i)\right) \propto p(\boldsymbol{\Theta}_r)N\left(g_{i,r}(\boldsymbol{x}_i)|m_{i,r}(\boldsymbol{x}_i),C_r(\boldsymbol{x}_i,\boldsymbol{x}_i')+\tau_r^2I\right)$$
(3)

where $p(\boldsymbol{\Theta}_r)$ is the prior distribution for the unknown parameters. The detailed specifications of $p(\boldsymbol{\Theta}_r)$ will be provided in the Case Study section. After obtaining the posterior distribution, one can predict the $\hat{g}_{new,r}(\boldsymbol{x}_{new})$ at a new process setting \boldsymbol{x}_{new} .

Evaluation of the density above involves computing the inverse and determinant of $C_r(x_i, x_i') + \tau_r^2 I$, which is computational intensive for large datasets [48]. Hence, a small set of m nearest neighbors of x_i rather than all samples are used in NNGP for the model estimation [48]

$$\{C_r(x_i, x_i') + \tau_r^2 I\}^{-1} \approx (I - A_r)^T D_r^{-1} (I - A_r), \tag{4}$$

where A_r is a sparse and lower triangular matrix with at most m non-zero entries in each row, and D_r is a diagonal matrix. The determinant of $\{C_r(x_i, x_i') + \tau_r^2 I\}$ equals to the determinate of D_r . Particularly, the non-zero elements, indexed by the corresponding m nearest neighbors of x_i in the i-th row of A_r , are used to exploit sparsity and reduce the computational complexity for model estimation [38], and are computed by [49]

$$A_r(i, N(x_i)) = C_r(x_i, N(x_i)) \{C_r(N(x_i), N(x_i)) + \tau_r^2 I\}^{-1},$$
 (5)

which are obtained by predicting $g_{i,r}(x_i)$ based on its neighborhood locations $N(x_i)$. The neighborhood is selected by the Euclidean distance [21]. The i-th diagonal of D_r is obtained by [49]

$$D_{r}(i,i) = C_{r}(\mathbf{x}_{i}, \mathbf{x}_{i}) + \tau_{r}^{2}$$

$$- C_{r}(\mathbf{x}_{i}, N(\mathbf{x}_{i})) \{ C_{r}(N(\mathbf{x}_{i}), N(\mathbf{x}_{i})) + \tau_{r}^{2} I \}^{-1} C_{r}(N(\mathbf{x}_{i}), \mathbf{x}_{i})$$
(6)

where $D_r(i,i)$ elements are the variance of $g_{i,r}(x_i)$ conditional on its neighbors in $g_{i,r}(N(x_i))$.

By constructing the sparse lower triangular matrix A_r (with no more than m non-zero entries in each row) and the diagonal matrix D_r , the inverse of the covariance matrix $\{C_r(x_i,x_i')+\tau_r^2I\}^{-1}$ is sparse and enjoys faster computation than GP. NNGP showed suitable probability distribution for values of neighborhood m between 10 and 20 [21].

Tensor Reconstruction and Comparison

The tensor response of the droplet solidification time T_{new} of a new process setting x_{new} can be predicted via tensor reconstruction. In particular, $\hat{g}_{new,r}(x_{new})$, $\forall r$

can be predicted from the individual NNGP models to form \hat{G}_{new} in the core tensor. We can then reconstruct $\hat{T}_{new} \approx [\hat{G}_{new}; U, V, W]$ based on the U, V and W learned from the joint tensor decomposition. The predicted \hat{T}_{new} will be compared with the simulated T_{new} from the physical model for the emulation model evaluation.

CASE STUDY

As mentioned in the Introduction section, the accurate and efficient evaluation of droplet solidification time will affect the determination of the waiting time among layers, and subsequently affect the printed part quality in FNP. For instance, Fig. 4 (b)-(c) shows the parts with proper and improper waiting times for the designed part in Fig. 4 (a). In this section, we demonstrate the proposed framework for the accurate and efficient prediction of droplet solidification time in FNP.

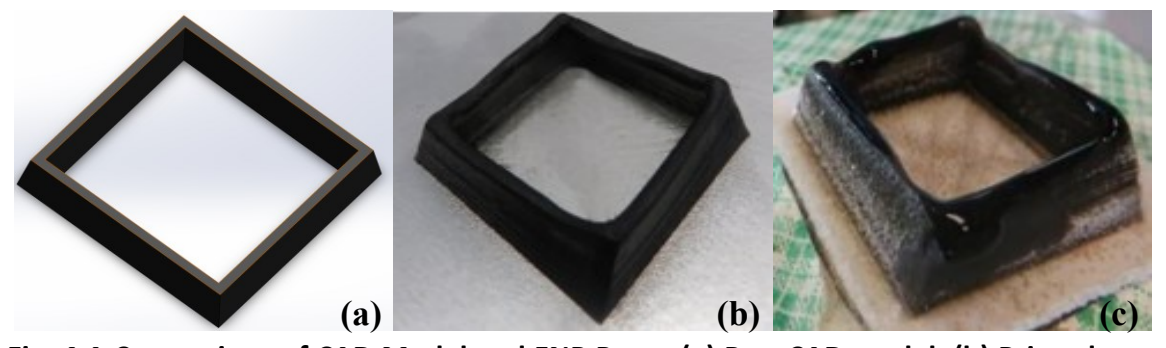


Fig. 4 A Comparison of CAD Model and FNP Parts: (a) Part CAD model, (b) Printed part with proper droplet solidification time, and (c) Printed part with improper droplet solidification time

To demonstrate the proposed framework, we simulate a single layer FNP part with 10 by 10 droplets modified from the physical model in [14]. Other more complicated shapes can be modeled similarly with the proposed framework. Fig. 5 shows the simulation setup. The deposited droplets have an initial temperature of 5 $^{\circ}C$ and are

ejected based on the path specified in Fig. 5 (b). After the ejection (Fig. 5 (a)), the droplets solidify in a short time due to the heat conduction with the heat sink (at -20 °C) under the build bed and heat convection with the ambient (Fig. 5 (c)). The corresponding droplet solidification time (time required for a droplet to cool down from 5 °C to -19 °C in this paper) is summarized as shown in Fig. 5 (d). In the simulation, we vary six process settings that will affect the thermal distribution. The names and ranges (lower and upper bounds) of these settings are shown in Table 1. In particular, the specific heat (X_1), density (X_3), interface heat transfer coefficient (X_5), and element heat transfer coefficient (X_6) are the material properties in the physical model representing how much heat the droplets

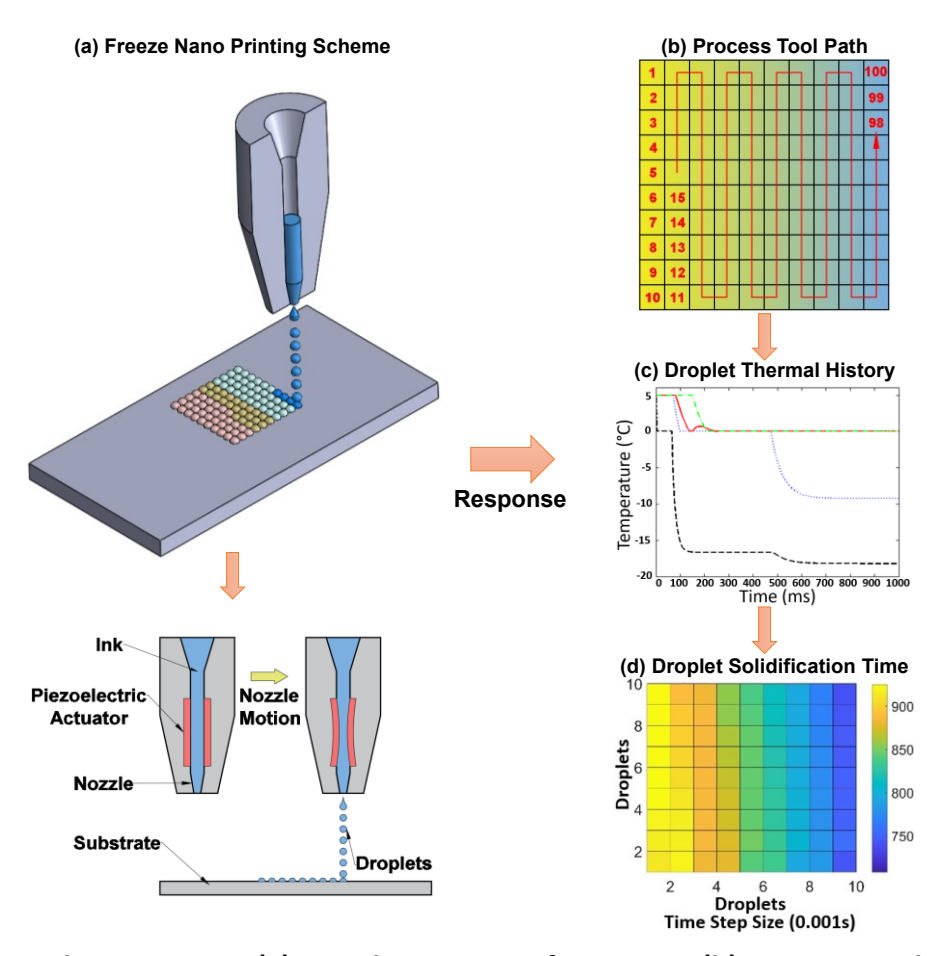


Fig. 5 Simulation Setup: (a) Droplet ejection from FNP, (b) Process tool path, (c) Examples of droplet thermal history, and (d) Summarized droplet solidification time

absorb, the concentration, and the rate of heat transfer. On the other hand, frequency (X_2) and layer thickness (X_4) are process parameters adjustable in the printing process. For our previous study in [45], we used 60 simulation runs to perform the GP emulation from the physical model. However, according to the model evaluation [45], the predicted results were not accurate enough (average Normalized Root Mean Squared Error (NRMSE) NRMSE = 11.59% in 5-fold Cross Validation (CV)). One of the most effective approach to improve the model performance is to increase the sample size (i.e., the number of simulation runs. Therefore, we generate 500 simulation runs from the physical model in this work. In these simulation runs, the process settings are determined by a Latin hypercube sampling-based space filling design [50].

Table 1 Simulation Process Settings and Ranges for the Case Study

IDs	Parameters	Lower Bounds	Upper Bounds
X_1	Specific heat $J/(kg \cdot K)$	3350	3450
X_2	Frequency (Hz)	50	500
X_3	Density (kg/m^3)	1000	1300
X_4	Layer thickness (mm)	0.1	0.6
X_5	Interface heat transfer coefficient $(W/m^2 \cdot K)$	200	500
X_6	Element heat transfer coefficient $(W/m^2 \cdot K)$	50	150

We then apply the proposed framework to the simulation data from these runs. During the model training, the simulated samples are divided into five randomly generated and equally sized folds for CV. In iterations, four out of the five folds are used for model training and the remaining fold is used for model testing. Training and testing iterations are repeated for five times. During the model training, the rank R in the joint tensor decomposition varies from 10%, 20%, up to 90% of the total tensor dimension and the final rank is selected to keep the proportion of the explained variation not less

than 99.5% of the total variation of the droplet solidification time in any process settings, i.e., $\min_i \|G_i; U, V, W\|_F / \|T_i\|_F \ge 99.5\%$. 99.5% is used here to preserve majority of the variation, and other threshold values such as 95% can also be used in other applications. For the joint tensor decomposition in our case, the selected rank R is 3 or 4, depending on the training and testing CV folds. After the determination of tensor rank R and the learning of the factorization matrices U, V and W, these factorization matrices are applied to the samples in the left-out CV fold to learn the core tensors. The corresponding core tensor entries will be used as the testing data for the NNGP model evaluation. m=20 is used as the number of nearest neighbor of x_i in NNGP.

For the NNGP model training for Eq. (2), we have each core tensor entries (e.g., the r-th entry $g_{i,r}$, $\forall i$) in the training data as the outputs and the corresponding process settings as inputs x. In Eq. (2), the prior distributions for $\beta_{r,j}$, τ_r and σ_r are set as Gaussian and the prior distribution for $\phi_{r,j}$ is set as inverse gamma. During the MCMC estimation of these NNGP model parameters, we have in total 5,000 iterations. Among these 5,000 iterations, 2,000 iterations are used for burn-in (i.e., the burn-in iterations will be discarded to stabilize the posterior distribution). After the burn-in, the MCMC mixed well, which indicates that the posterior distributions converge. We then use the last 3,000 MCMC iterations for the model prediction at certain process settings. Particularly, we calculate the mean of the predicted $\hat{g}_{new,r}(x_{new})'s$ from 3,000 posterior draws. The above procedures are repeated for all $r=1,\cdots,R$. We then organize the predicted $\hat{G}_{new}={\rm diag}(\hat{g}_{new,1},\hat{g}_{new,2},\cdots,\hat{g}_{new,R})$, and perform the tensor reconstruction introduced in the Proposed Method section.

We then compare the model performance of NNGP with alternative tensor response regression approaches: STORE, OLS, Sparse OLS, and HOLRR. For the alternative models, [24] considers the tensor response regression model of the form

$$T_i = \mathbf{B}^* \times_{a+1} x_i + \varepsilon_i, \tag{7}$$

where $T_i \in R^{d_1 \times \cdots \times d_q}$ is an qth-order tensor response (droplet solidification time in our case), $\mathbf{x}_i \in R^p$ is a vector of predictors (i.e., specific heat, frequency, etc.), $\mathbf{B}^* \in R^{d_1 \times \cdots \times d_q \times p}$ is an (q+1)th-order tensor coefficient, and $\varepsilon_i \in R^{d_1 \times \cdots \times d_q}$ is an error tensor independent of \mathbf{B}^* . The ultimate goal is to estimate \mathbf{B}^* given observations $\{(\mathbf{x}_i, T_i), i = 1, \dots, n\}$. Once the tensor coefficient \mathbf{B}^* is estimated, the new solidification time \widehat{T}_{new} for \mathbf{x}_{new} can be obtained by evaluating $\widehat{T}_{new} = \widehat{\mathbf{B}}^* \times_{q+1} \mathbf{x}_{new}$ [51].

Identically to what we applied in the proposed framework, we utilize the same equally sized five folds for CV (referred as outer-CV hereafter) for the alternative models. In particular, four folds are taken for model training and the remaining fold is deployed for model testing, and the process is repeated for in total five iterations. For the STORE framework [24], the tuning parameters rank and sparsity need to be determined. We set the $rank = \{1, 2, ..., 10\}$ and $sparsity = \{0.1, 0.2, ..., 1\}$, where sparsity refers to the proportion of significant coefficients in \mathbf{B}^* [24]. Another CV (referred to as inner-CV hereafter) is used for the selection of these tuning parameters. Specifically, the training samples in the outer-CV (i.e., the four folds used in model training) is equally divided into five folds again. In iterations, we train STORE with four out of the five inner-CV folds at each tuning parameter combination, and test its performance with the left-out inner-CV fold. We then average the testing errors at all tuning parameter combinations over the

five inner-CV iterations, and select the best tuning parameter combination of rank and sparsity with the smallest average testing error. With the selected tuning parameter combination, we train the model with the training samples (the four folds used in model training) in the outer-CV, and evaluate the model with the left-out folder in the outer-CV similar to NNGP. Sparse OLS and HOLRR are compared similarly, see [25] and [26], respectively, for details.

The mean NRMSE prediction error and its standard deviation over five CV folds for NNGP and alternative models are presented in Fig. 6. The NRMSE is calculated via $\sum_i \left\|T_i - \widehat{T}_i\right\|_F / \sum_i \left\|T_i\right\|_F, \text{ where } T_i \text{ is the true simulated solidification time and } \widehat{T}_i \text{ is the predicted solidification time. From Fig. 6, the proposed method can capture the variations in the solidification time with accurate predictions (a small NRMSE). While the NRMSE in STORE is considerably higher compared to the NRMSE in NNGP. On the other hand, OLS, Sparse OLS, and HOLRR performed a little better than STORE, but still do not perform as$

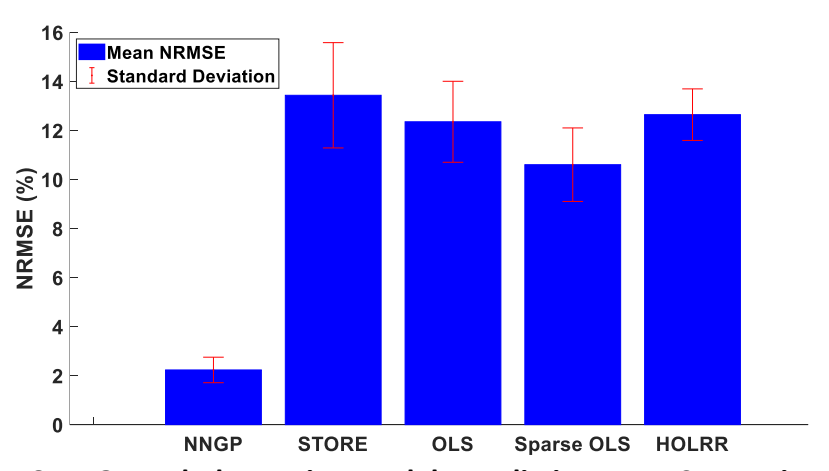


Fig. 6 NNGP and Alternative Models Prediction Error Comparison

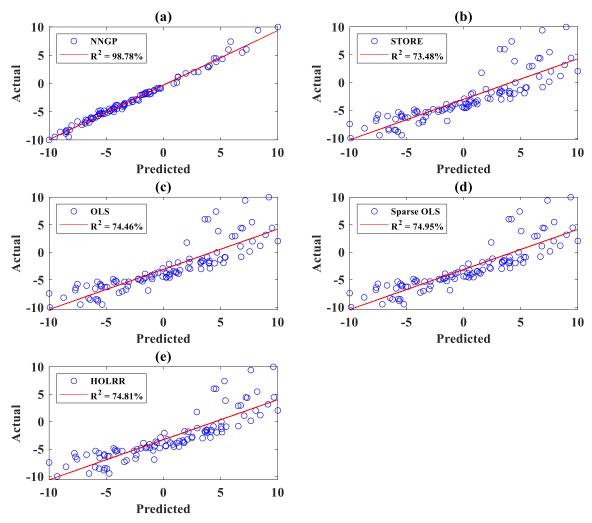


Fig. 7 Normalized Frobenius Norm of the Actual Values Versus Predicted Values: (a) NNGP, (b) STORE, (c) OLS, (d) Sparse OLS, and (e) HOLRR

good as our proposed framework. To compare the models, Fig. 7 shows the relationship between the normalized Frobenius norm (normalized to the range of [-10, 10]) of actual values (i.e., true simulated solidification time) and predicted values (i.e., predicted solidification time) for all the NNGP and alternative models, and the corresponding R^2 value. It can also be observed that the Sparse OLS model ($R^2 = 74.95\%$) stands out from the other alternatives, while the NNGP model performs the best ($R^2 = 98.78\%$). To

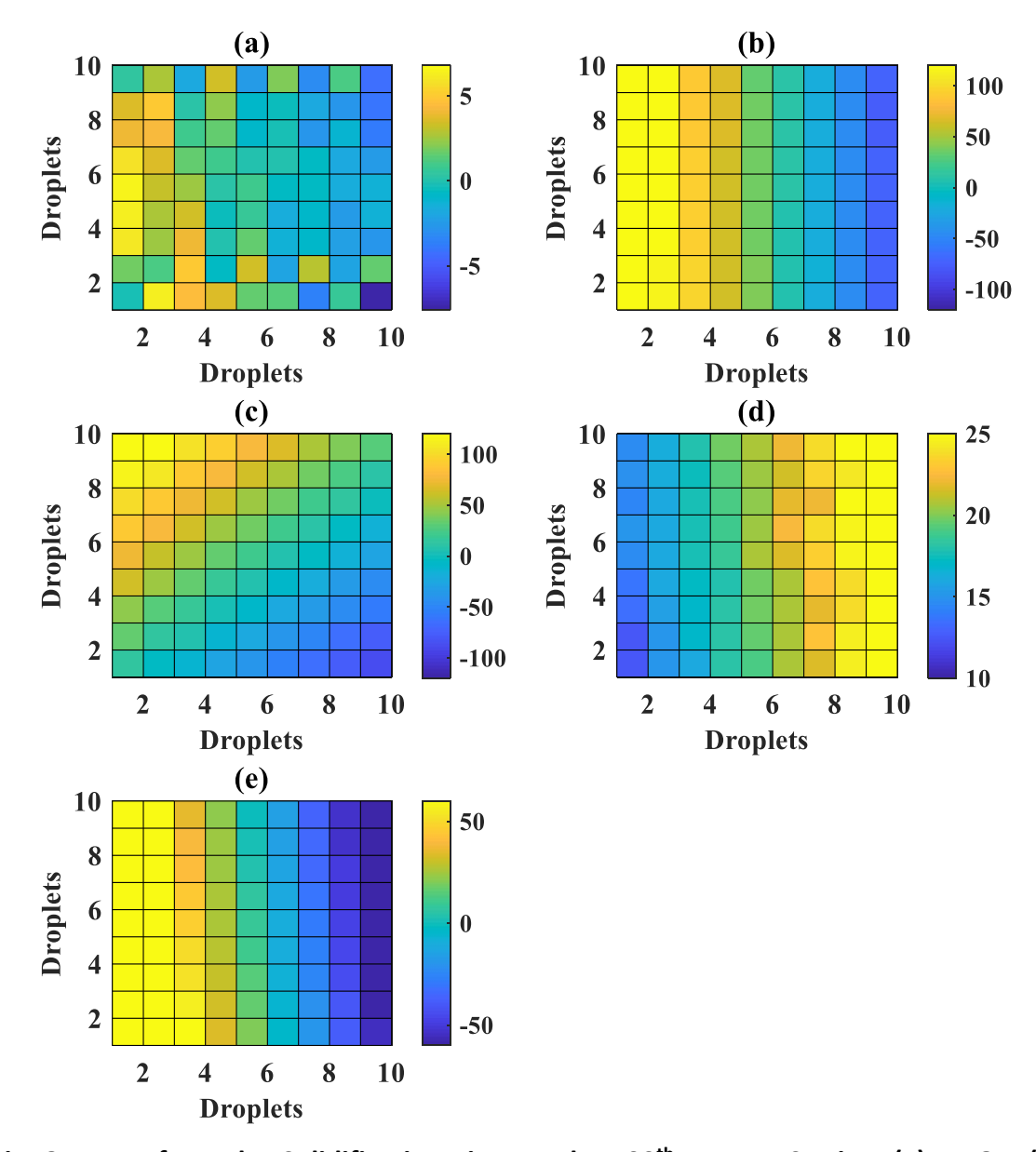


Fig. 8 Error of Droplet Solidification Time at the 500th Process Setting: (a) NNGP, (b) STORE, (c) OLS, (d) Sparse OLS, and (e) HOLRR

further assess the prediction of solidification time at a certain process setting, Fig. 8 shows the error of droplet solidification time at the 500th process settings for the NNGP and alternative models (in terms of the simulation step size, where each step is 0.001 s). According to the figures, the NNGP has more accurate predictions than alternative tensor

response regression models, due to its capability of capturing the nonlinear relationships between the process settings and droplet solidification time.

Moreover, the NNGP model prediction for a new sample can be performed in around 0.2 seconds. This is much faster than running physical model, which can take several minutes for a simple shape. Meanwhile, the NNGP can accurately emulate the physical model. Thus, the proposed framework can facilitate the future real-time process optimization and control.

CONCLUSION AND DISCUSSION

FNP is a novel technique capable to produce macroscale and microscale features, thus advancing the 3D printing of energy products. Particularly, FNP can increase the power density and energy density of energy storage devices (e.g., batteries and supercapacitors). However, the quality, integrity, and repeatability of the printed energy storage devices from FNP are not fully considered. In FNP, thermal management, which is dependent on the process settings, governs the droplet solidification time and subsequently the waiting time between layers. Studying the droplet solidification time by trial-and-error approach is impractical due to the high material costs. Physical models are an alternative, where the droplet solidification time can be simulated. Nevertheless, their computation is expensive, which prevents their utilization for real-time prediction and process optimization. In this work, we explore machine-learning methods to address the prediction of high dimensional solidification time for future real-time process optimization and control. We integrate joint tensor decomposition, NNGP model, and the physical model outputs in our proposed framework. The novelty of this paper lays on the

effective representation of the tensor responses by low dimensional vectors and the core tensor, and the modeling can be performed separately for the independent elements in the core tensor based on NNGP models. The proposed framework can not only build an efficient and accurate emulator for the prediction of the solidification time under new process settings, but also properly captures the nonlinear relationships between process settings and tensor responses (i.e., droplet solidification time). It is demonstrated that the NNGP emulator outperformed the accuracy of alternative models, namely STORE, OLS, Sparse OLS, and HOLRR. The framework can be applied to problems with high dimensional output in additive manufacturing and has broad applications.

There are several potential research directions that can be pursued. One direction is to extend this framework to smartly determine the number of neighbors rather than just use m for all samples and develop a fully Bayesian approach for the tensor response prediction. Another direction is to model the layer-wise evolution considering the layer correlations. Also, before implementing the proposed framework for the real-time process control and optimization, it is necessary to validate the model with physical experiments. Hence, we will take the thermal measurement from the FNP process and perform the model calibration. We will ultimately use the calibrated model for the process optimization and control so that we can adjust the waiting time and process parameters during the printing.

ACKNOWLEDGEMENT

This work is partially supported by the NSF grants # CMMI-1846863 and Sustainable Manufacturing and Advanced Robotics Technologies, Community of Excellence (SMART CoE) at State University of New York at Buffalo.

NOMENCLATURE

T	Raw tensor data	
$ ilde{T}^{CP}$	Approximated tensor data after Candecomp/Parafac decomposition	
$ ilde{T}^{Tucker}$	Approximated tensor data after Tucker decomposition	
U	Factorization matrix, where $U \in R^{I \times R}$	
V	Factorization matrix, where $V \in R^{J \times R}$	
W	Factorization matrix, where $W \in R^{K \times R}$	
G	Core tensor after decomposition	
x	A vector of physical model inputs	
$m_{i,r}(\mathbf{x})$	Mean function of rank r corresponding to i^{th} sample at $oldsymbol{x}$	
$oldsymbol{eta}_r$	The model parameters for the mean effect of rank \boldsymbol{r}	
$\omega_{i,r}(\mathbf{x})$	A stochastic process, which follows a $\mathit{GP} ig(0, \mathit{C}_r(x, x') ig)$ with mean 0 and	
	covariance $\mathcal{C}_r(\pmb{x},\pmb{x}')$	
$\varepsilon_{i,r}(\mathbf{x})$	Error, which follows a $N(0, au_r^2)$ with mean 0 and variance $ au_r^2$	
$\phi_{r,j}$	Weight adjustment parameter of each direction j	
σ_r^2	Scaling parameter	
m	Number of nearest neighbors	
A_r	A sparse and lower triangular matrix of rank \boldsymbol{r}	
D_r	A diagonal matrix of rank r	

 $m{ heta}_r$ Unknown parameters of rank r Prior distribution for the unknown parameters of rank r $\hat{\lambda}_{new,r}(x_{new})$ Predicted core tensor at new process settings x_{new} Tensor response of the droplet solidification time at new process settings x_{new} Predicted tensor response of the droplet solidification time at new process settings x_{new}

REFERENCES

- [1] C. Lethien, J. Le Bideau, and T. Brousse, "Challenges and prospects of 3D microsupercapacitors for powering the internet of things," *Energy & Environmental Science*, vol. 12, no. 1, pp. 96-115, 2019.
- [2] G. Zubi, R. Dufo-Lopez, M. Carvalho, and G. Pasaoglu, "The lithium-ion battery: state of the art and future perspectives," *Renewable and Sustainable Energy Reviews,* vol. 89, pp. 292-308, 2018.
- [3] N. R. Council, "Meeting the energy needs of future warriors," *National Academies*Press, 2004.
- [4] X. Pu, W. Hu, and Z. L. Wang, "Toward wearable self-charging power systems: the integration of energy-harvesting and storage devices," *Small*, vol. 14, no. 1, pp. 1702817, 2018.
- [5] Y. Huang, Y. Zeng, M. Yu, P. Liu, Y. Tong, F. Cheng, and X. Lu, "Recent smart methods for achieving high-energy asymmetric supercapacitors," *Small Methods*, vol. 2, no. 2, pp. 1700230, 2018.
- [6] K. Shen, J. Ding, and S. Yang, "3D printing quasi-solid-state asymmetric microsupercapacitors with ultrahigh areal energy density," *Advanced Energy Materials*, vol. 8, no. 20, pp. 1800408, 2018.
- [7] B. Berman, "3-D printing: the new industrial revolution," *Business Horizons*, vol. 55, no. 2, pp. 155-162, 2012.

- [8] K. Fu, Y. Wang, C. Yan, Y. Yao, Y. Chen, J. Dai, and Z. Wang, "Graphene oxide-based electrode inks for 3D-printed lithium-ion batteries," *Advanced Materials*, vol. 28, no. 23, pp. 2587-2594, 2016.
- [9] M. Areir, Y. Xu, D. Harrison, and J. Fyson, "3D printing of highly flexible supercapacitor designed for wearable energy storage," *Materials Science and Engineering*, vol. B, no. 226, pp. 29-38, 2017.
- [10] F. Zhang, M. Wei, V. V. Viswanathan, B. Swart, Y. Shao, G. Wu, and C. Zhou, "3D printing technologies for electrochemical energy storage," *Nano Energy*, vol. 40, pp. 418-431, 2017.
- [11] F. Zhang, F. Yang, D. Lin, and C. Zhou, "Parameter study of three-dimensional printing graphene oxide based on directional freezing," *Journal of Manufacturing Science and Engineering*, vol. 139, no. 3, pp. 031016, 2017.
- [12] Q. Zhang, F. Zhang, S. P. Medarametla, H. Li, C. Zhou, and D. Lin, "3D printing of graphene aerogels," *Small*, vol. 12, no. 13, pp. 1702-1708, 2016.
- [13] H. Bikas, P. Stavropoulus, and G. Chryssolouris., "Additive manufacturing methods and modelling approaches: a critical review," *International Journal of Advanced Manufacturing Technology*, vol. 83, no. 1-4, pp. 389-405, 2016.
- [14] G. Zhao, C. Zhou, and D. Lin, "Thermal analysis on directional freezing of nano aqueous suspensions in graphene aerogel 3D printing process," *ASME 2016 11th International Manufacturing Science and Engineering Conference*, pp. V003T08A011-V003T08A011, 2016.

- [15] K. MC and O. A., "Bayesian calibration of computer models," *Journal of the Royal Statistical Society: Series B (Statistical Methodology)*, vol. 63, no. 3, pp. 425-64, 2001.
- [16] D. Higdon, J. Gattiker, B. Williams, and M. Rightley, "Computer model calibration using high-dimensional output," *Journal of the American Statistical Association*, vol. 103, no. 482, pp. 570-583, 2008.
- [17] S. Mak, C. L. Sung, X. Wang, S. T. Yeh, Y. H. Chang, V. R. Joseph, and C. J. Wu, "An efficient surrogate model for emulation and physics extraction of large eddy simulations," *Journal of the American Statistical Association*, vol. 113, no. 524, pp. 1443-1456, 2018.
- [18] N. D. Sidiropoulos, L. De Lathauwer, X. Fu, K. Huang, E. E. Papalexakis, and C. Faloutsos, "Tensor decomposition for signal processing and machine learning," *IEEE Transactions on Signal Processing*, vol. 65, no. 13, pp. 3551-3582, 2017.
- [19] M. Sørensen and L. D. De Lathauwer, "Coupled canonical polyadic decompositions and (coupled) decompositions in multilinear rank-(L_r,n,L_r,n,1) terms---part I: uniqueness.," *SIAM Journal on Matrix Analysis and Applications,* vol. 36, no. 2, pp. 496-522, 2015.
- [20] R. C. Farias, J. E. Cohen, and P. Comon, "Exploring multimodal data fusion through joint decompositions with flexible couplings," *IEEE Transactions on Signal Processing*, vol. 64, no. 18, pp. 4830-4844, 2016.

- [21] A. Datta, S. Banerjee, A. O. Finley, and A. E. Gelfand, "Hierarchical nearest-neighbor Gaussian process models for large geostatistical datasets," *Journal of the American Statistical Association*, vol. 111, no. 514, pp. 800-812, 2016.
- [22] P. Yuan and D. Gu, "Molten pool behaviour and its physical mechanism during selective laser melting of TiC/AlSi10Mg nanocomposites: simulation and experiments," *Journal of Physics D: Applied Physics*, vol. 48, no. 3, pp. 035303, 2015.
- [23] H. C. Wu, H. J. Lin, Y. C. Kuo, and W. S. Hwang, "Simulation of droplet ejection for a piezoelectric inkjet printing device," *Materials Transactions*, vol. 45, no. 3, pp. 893-899, 2004.
- [24] W. W. Sun and L. Li, "STORE: sparse tensor response regression and neuroimaging analysis," *The Journal of Machine Learning Research*, vol. 18, no. 1, pp. 4908-4944, 2017.
- [25] J. Peng, J. Zhu, A. Bergamaschi, W. Han, D. Y. Noh, J. R. Pollack, and P. Wang, "Regularized multivariate regression for identifying master predictors with application to integrative genomics study of breast cancer," *The Annals of Applied Statistics*, vol. 4, no. 1, pp. 53, 2010.
- [26] G. Rabusseau and H. Kadri, "Low-rank regression with tensor responses," *Advances in Neural Information Processing Systems*, pp. 1867-1875, 2016.
- [27] K. Sun, T. S. Wei, B. Y. Ahn, J. Y. Seo, S. J. Dillon, and J. A. Lewis, "3D printing of interdigitated li-ion microbattery architectures," *Advanced Materials*, vol. 25, no. 33, pp. 4539-4543, 2013.

- [28] K. Fu, Y. Wang, C. Yan, Y. Yao, Y. Chen, J. Dai, and Z. Wang, "Graphene oxide-based electrode inks for 3D-printed lithium-ion batteries," *Advanced Materials*, vol. 28, no. 13, pp. 2587-2594, 2016.
- [29] C. Zhu, T. Liu, F. Qian, T. Y. J. Han, E. B. Duoss, J. D. Kuntz, and Y. Li, "Supercapacitors based on three-dimensional hierarchical graphene aerogels with periodic macropores," *Nano Letters*, vol. 16, no. 6, pp. 3448-3456, 2016.
- [30] M. Areir, Y. Xu, D. Harrison, and J. Fyson, "3D printing of highly flexible supercapacitor designed for wearable energy storage," *Materials Science and Engineering: B*, no. 226, pp. 29-38, 2017.
- [31] J. Liu, C. Liu, Y. Bai, P. Rao, C. B. Williams, and Z. Kong, "Layer-wise spatial modeling of porosity in additive manufacturing," *IISE Transactions*, vol. 51, no. 2, pp. 109-123, 2019.
- [32] G. Tapia, A. H. Elwany, and H. Sang, "Prediction of porosity in metal-based additive manufacturing using spatial Gaussian process models," *Additive Manufacturing*, vol. 12, pp. 282-290, 2016.
- [33] Q. Huang, J. Zhang, A. Sabbaghi, and T. Dasgupta, "Optimal offline compensation of shape shrinkage for three-dimensional printing processes," *IIE Transactions*, vol. 47, no. 5, pp. 431-441, 2015.
- [34] M. S. Tootooni, A. Dsouza, R. Donovan, P. K. Rao, Z. J. Kong, and P. Borgesen, "Classifying the dimensional variation in additive manufactured parts from laser-

- scanned three-dimensional point cloud data using machine learning approaches," *Journal of Manufacturing Science and Engineering*, vol. 139, no. 9, pp. 091005, 2017.
- [35] F. Liravi, R. Darleux, and E. Toyserkani, "Additive manufacturing of 3D structures with non-Newtonian highly viscous fluids: finite element modeling and experimental validation," *Additive Manufacturing*, vol. 13, pp. 113-123, 2017.
- [36] J. Li, R. Jin, and Z. Y. Hang, "Integration of physically-based and data-driven approaches for thermal field prediction in additive manufacturing," *Materials & Design*, vol. 139, pp. 473-485, 2018.
- [37] H. Sun, G. Pedrielli, G. Zhao, A. Bragagnolo, C. Zhou, R. Pan, and W. Xu, "Cyber-coordinated simulation models for multi-stage additive manufacturing of energy products," In 2018 IEEE 14th International Conference on Automation Science and Engineering (CASE), pp. 893-898, 2018.
- [38] A. Datta, S. Banerjee, A. O. Finley, and A. E. Gelfand, "On nearest-neighbor Gaussian process models for massive spatial data," *Wiley Interdisciplinary Reviews:*Computational Statistics, vol. 8, no. 5, pp. 162-171, 2016.
- [39] I. V. Oseledets, "Tensor-train decomposition," *SIAM Journal on Scientific Computing,* vol. 33, no. 5, pp. 2295-2317, 2011.
- [40] H. Yan, K. Paynabar, and M. Pacella, "Structured point cloud data analysis via regularized tensor regression for process modeling and optimization," *Technometrics*, pp. 1-36, 2018.

- [41] M. S. Tootooni, A. Dsouza, R. Donovan, P. K. Rao, Z. J. Kong, and P. Borgesen, "Assessing the geometric integrity of additive manufactured parts from point cloud data using spectral graph theoretic sparse representation-based classification," *In ASME 2017 12th International Manufacturing Science and Engineering Conference collocated with the JSME/ASME 2017 6th International Conference on Materials and Processing*, pp. V002T01A042-V002T01A042, 2017.
- [42] H. Yan, K. Paynabar, and J. Shi, "Image-based process monitoring using low-rank tensor decomposition," *IEEE Transactions on Automation Science and Engineering*, vol. 12, no. 1, pp. 216-227, 2015.
- [43] N. Vervliet, O. Debals, and L. De Lathauwer, "Tensorlab 3.0—Numerical optimization strategies for large-scale constrained and coupled matrix/tensor factorization," *In* 2016 50th Asilomar Conference on Signals, Systems and Computers, pp. 1733-1738, 2016.
- [44] S. Zhou and J. Jin, "Automatic feature selection for unsupervised clustering of cycle-based signals in manufacturing processes," *IIE Transactions*, vol. 37, no. 6, pp. 569-584, 2005.
- [45] L. J. Segura, G. Zhao, H. Sun, and C. Zhou, "Gaussian process tensor responses emulation for droplet solidification in freeze nano 3D printing of energy products," submitted to ASME 2019 14th International Manufacturing Science and Engineering Conference, Accepted, 2019.

- [46] A. V. Vecchia, "Estimation and model identification for continuous spatial processes," *Journal of the Royal Statistical Society: Series B (Methodological)*, vol. 50, no. 2, pp. 297-312, 1988.
- [47] C. E. Rasmussen, "Gaussian processes in machine learning," In *Summer School on Machine Learning*, Heidelberg, Berlin: Springer, 2003.
- [48] A. O. Finley, A. Datta, B. D. Cook, D. C. Morton, H. E. Andersen, and S. Banerjee, "Efficient algorithms for bayesian nearest-neighbor Gaussian processes," *Journal of Computational and Graphical Statistics*, pp. 1-14, 2019.
- [49] L. Zhang, A. Datta, and S. Banerjee, "Practical bayesian modeling and inference for massive spatial data sets on modest computing environments," *Statistical Analysis* and Data Mining: The ASA Data Science Journal, vol. 12, no. 3, pp. 197-209, 2019.
- [50] T. J. Santner, B. J. Williams, W. Notz, and B. J. Williams, "The design and analysis of computer experiments," New York, NY: Springer, 2003.
- [51] T. G. Kolda and B. W. Bader, "Tensor decompositions and applications," *SIAM Review*, vol. 51, no. 3, pp. 455-500, 2009.

Figure Captions List

Fig. 1	An Illustration of the Freeze Nano Printing Process
Fig. 2	An Illustration of the Proposed Framework
Fig. 3	A Schematic Illustration of the Joint Tensor Decomposition
Fig. 4	A Comparison of CAD Model and FNP Parts
Fig. 5	Simulation Setup
Fig. 6	NNGP and Alternative Models Prediction Error Comparison
Fig. 7	Frobenius Norm of the Actual Values Versus Predicted Values
Fig. 8	Error of Droplet Solidification Time at the 500^{th} Process Setting

Table Caption List

Table 1 Simulation Process Settings and Ranges for the Case Study

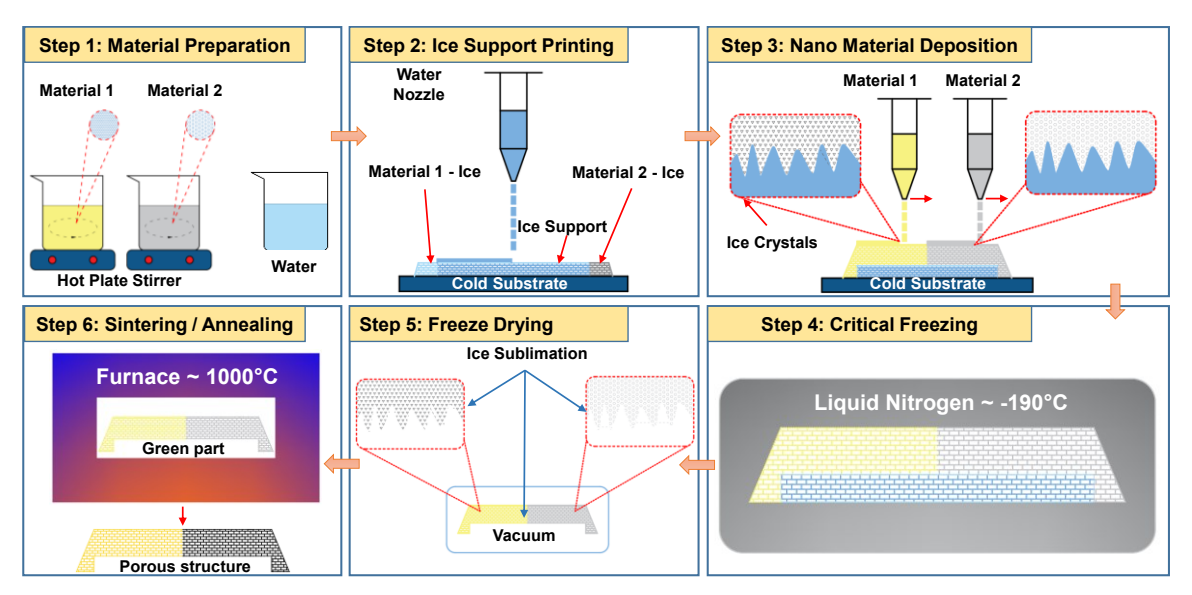


Fig. 1 An Illustration of the Freeze Nano Printing Process [10]

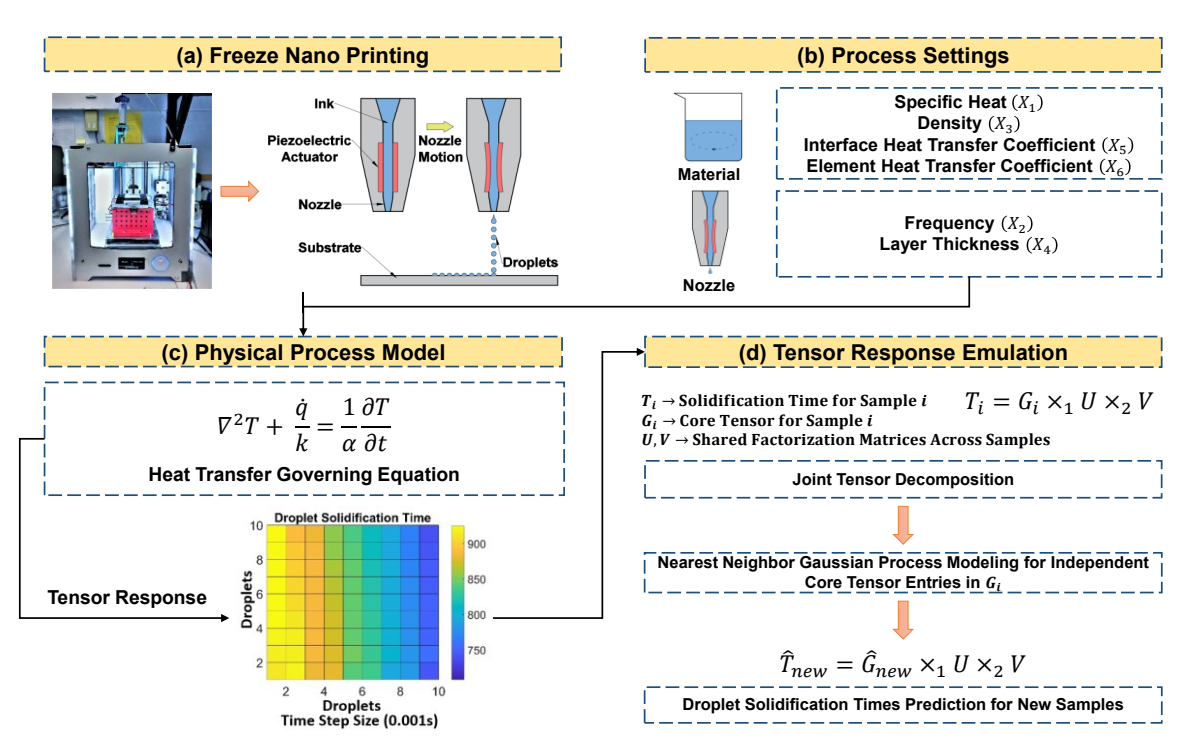


Fig. 2 An Illustration of the Proposed Framework: (a) Scheme of the FNP setup, (b) Process settings for the physical model input simulation, (c) Physical heat transfer process model, and (d) Tensor response modeling via joint tensor decomposition and NNGP

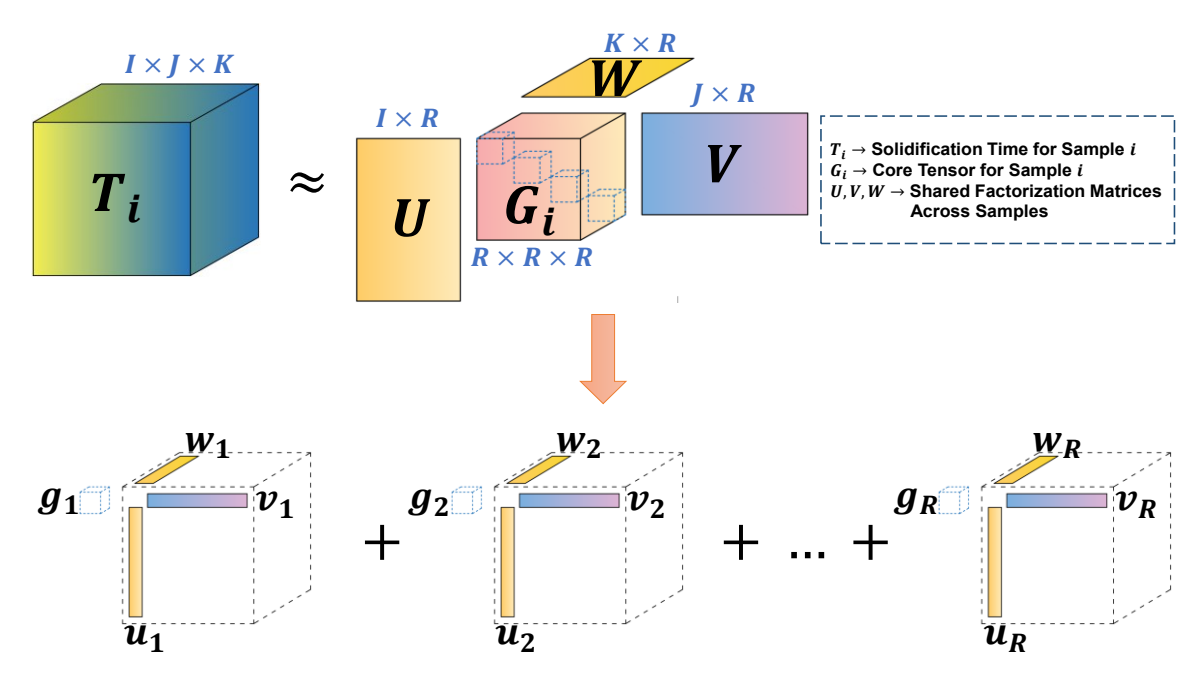


Fig. 3 A Schematic Illustration of the Joint Tensor Decomposition

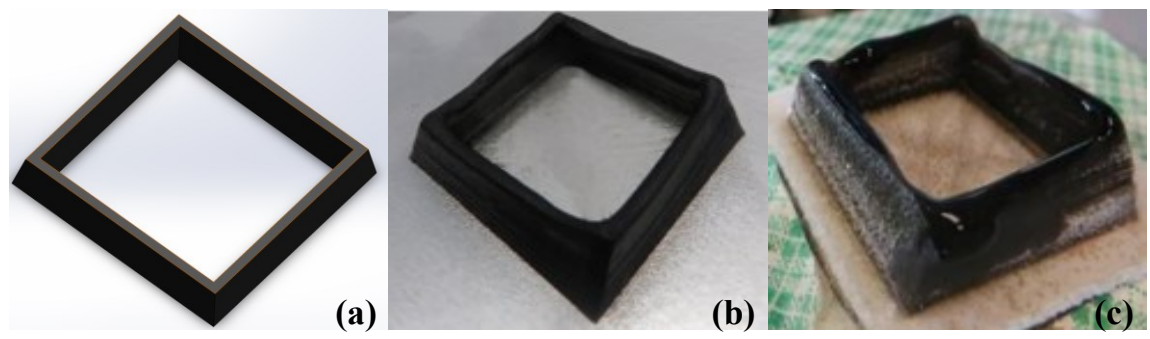


Fig. 4 A Comparison of CAD Model and FNP Parts: (a) Part CAD model, (b) Printed part with proper droplet solidification time, and (c) Printed part with improper droplet solidification time

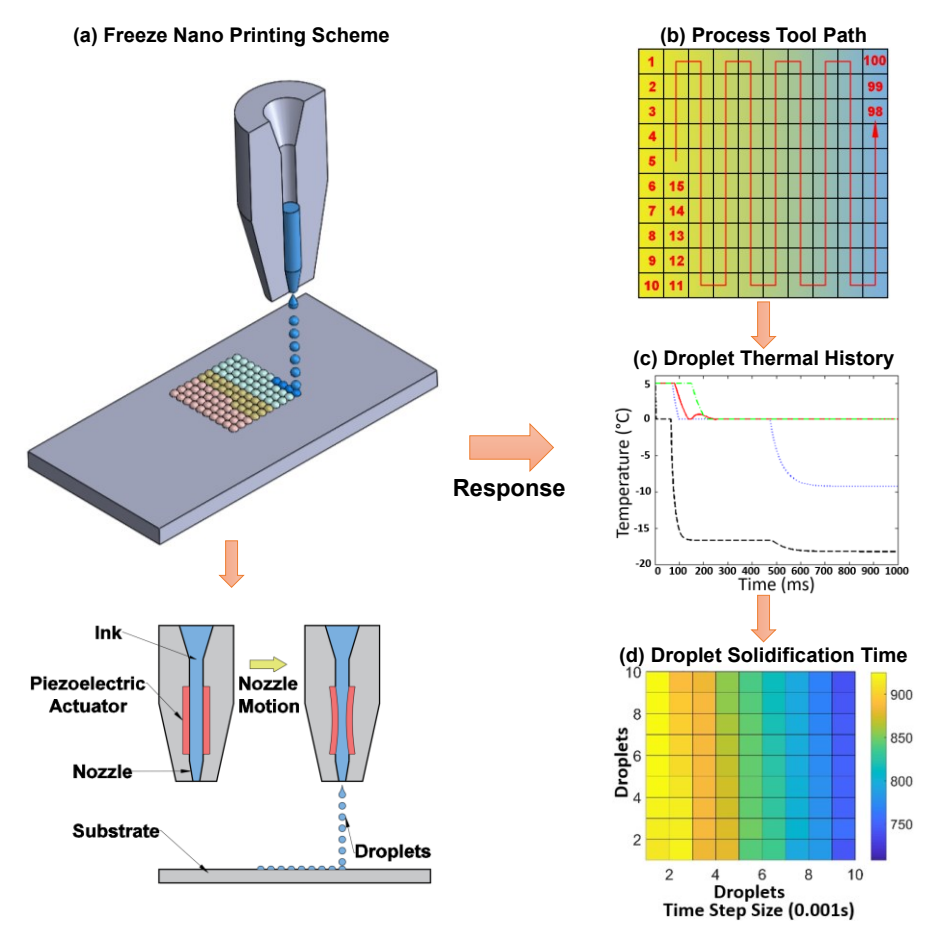


Fig. 5 Simulation Setup: (a) Droplet ejection from FNP, (b) Process tool path, (c) Examples of droplet thermal history, and (d) Summarized droplet solidification time

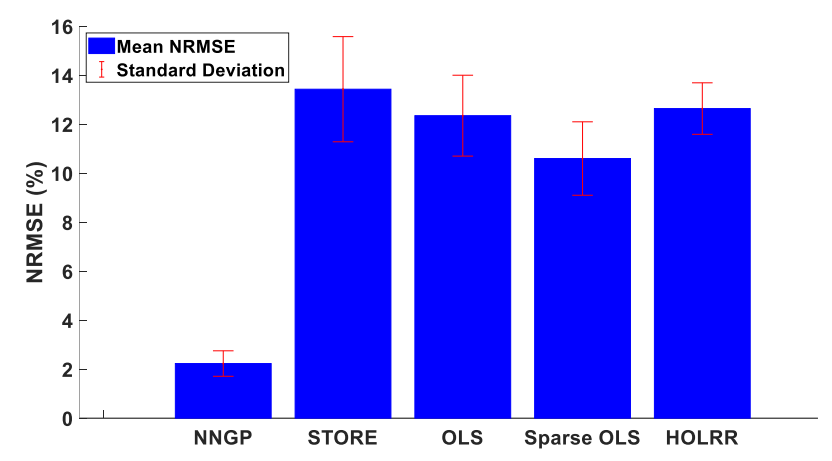


Fig. 6 NNGP and Alternative Models Prediction Error Comparison

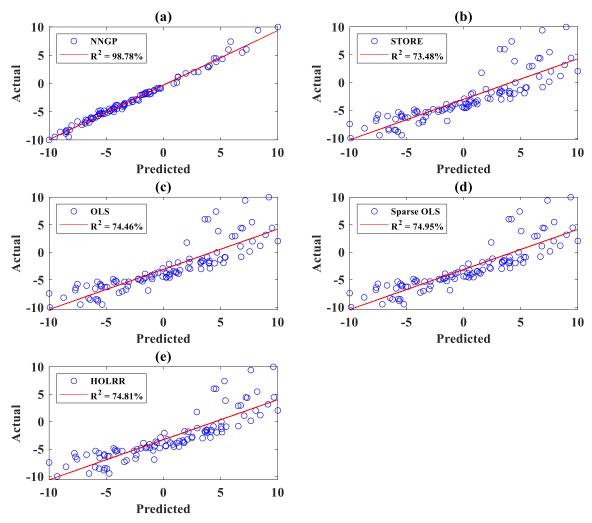


Fig. 7 Normalized Frobenius Norm of the Actual Values Versus Predicted Values: (a) NNGP, (b) STORE, (c) OLS, (d) Sparse OLS, and (e) HOLRR

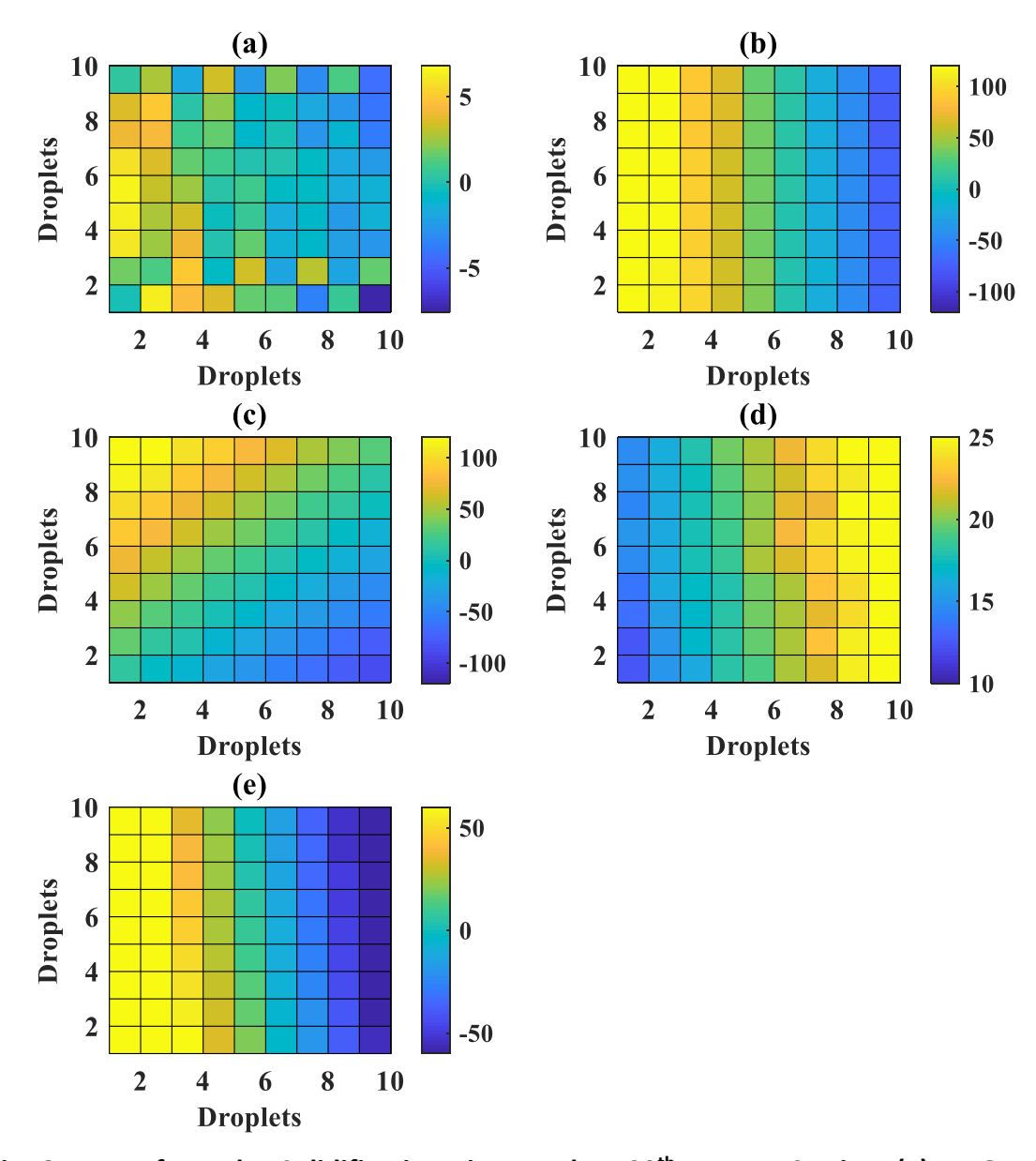


Fig. 8 Error of Droplet Solidification Time at the 500th Process Setting: (a) NNGP, (b) STORE, (c) OLS, (d) Sparse OLS, and (e) HOLRR

Table 1 Simulation Process Settings and Ranges for the Case Study

IDs	Parameters	Lower Bounds	Upper Bounds
X_1	Specific heat $J/(kg\cdot K)$	3350	3450
X_2	Frequency (Hz)	50	500
X_3	Density (kg/m^3)	1000	1300
X_4	Layer thickness (mm)	0.1	0.6
X_5	Interface heat transfer coefficient ($W/m^2 \cdot K$)	200	500
X_6	Element heat transfer coefficient ($W/m^2 \cdot K$)	50	150